Research Square

Preprints are preliminary reports that have not undergone peer review.
They should not be considered conclusive, used to inform clinical practice,
or referenced by the media as validated information.

Relating the thermodynamic warming response of precipitation and streamflows across the contiguous United States

Marc Prange

mp1506@princeton.edu

Princeton University

Ming Zhao

Geophysical Fluid Dynamics Laboratory

Elena Shevliakova

Geophysical Fluid Dynamics Laboratory

Sergey Malyshev

Geophysical Fluid Dynamics Laboratory

Minki Hong

Princeton University

Article

Keywords: streamflow, floods, warming, precipitation

Posted Date: May 15th, 2025

DOI: https://doi.org/10.21203/rs.3.rs-6631514/v1

License: This work is licensed under a Creative Commons Attribution 4.0 International License.
Read Full License

Additional Declarations: No competing interests reported.

Version of Record: A version of this preprint was published at npj Climate and Atmospheric Science on November 20th, 2025. See the published version at https://doi.org/10.1038/s41612-025-01257-9.

Relating the thermodynamic warming response of precipitation and streamflows across the contiguous United States

Marc Prange[1], Ming Zhao[2], Elena Shevliakova[2], Sergey Malyshev[2], Minki Hong[1]

[1]Atmospheric and Oceanic Sciences, Princeton University, Princeton, 08540, New Jersey, USA.
[2]Geophysical Fluid Dynamics Laboratory, NOAA, Princeton, 08540, New Jersey, USA.

Contributing authors: mp1506@princeton.edu; ming.zhao@noaa.gov; elena.shevliakova@noaa.gov; sergey.malyshev@noaa.gov; mh0093@princeton.edu;

Abstract

The relation of regional precipitation and streamflow changes with global warming is complicated by runoff often being the small residual in the balance between precipitation and evapotranspiration. In addition, the inhomogeneous nature of land-hydrological properties and hydrological interventions by humans, like irrigation and dams, have made streamflow sensitivities challenging to constrain with both climate models and observations. Here, we elucidate the hydrological processes driving the regionally varying mean and extreme streamflow sensitivities to warming across the contiguous United States in a counter-factual warming scenario using GFDL's moderately high-resolution global climate model. We show that over the west coast and eastern US atmospheric rivers are the dominant driver of high-flows in the present climate and of more frequent high-flows in a warmer climate. Over the mountainous western US, streamflows dwindle despite increases in precipitation and antecedent soil moisture as loss of snow fuels evapotranspiration at double the rate of precipitation changes.

Keywords: streamflow, floods, warming, precipitation

1 Introduction

Understanding how regional precipitation and river floods will respond to global warming is a crucial question for both climate science and society. At global scales strong constraints on precipitation changes with warming exist with an expected mean increase of 2-3 $\%\,K^{-1}$ [1–4], large-scale patterns following the paradigm of *wet gets wetter, dry gets drier* [1, 5–7] and an overall shift towards more extreme and less moderate precipitation events [8–15]; a change in the character of precipitation [16]. At regional scales, however, vast uncertainties remain due to the computational need to compromise between spatial resolution of climate models, long integration times and ensemble or domain sizes [14, 17–20].

While these constraints also limit predictability of changes in river floods with warming, precipitation is only one of a multitude of land-hydrological processes that determine flooding and its change with warming [21–24]. The amount of precipitation necessary to produce runoff is strongly determined by antecedent soil conditions, which are controlled by processes such as previous precipitation, snow-melt and evapotranspiration (ET) [25–28] that in climate models often require strong assumptions about the sub-grid scale. In addition, observational constraints on trends in river floods remain limited due to weak signal-to-noise ratios and human interventions [29, 30]. Hence, improving global coupled atmosphere-land models to higher resolutions offers an exciting opportunity to enhance our process understanding of precipitation and flood changes with warming.

Recent advances to moderately high resolutions of 50 km and higher driven through the CMIP6-HighResMIP initiative [31] have shown promising improvements in representing precipitation and its extremes [32–38], particularly in the mid-latitudes where mesoscale frontal systems dominate the spatial scales of precipitation [39, 40]. A strong contributor to mid-latitude precipitation and floods are Atmospheric Rivers (ARs) [14, 26, 41–44], which are characterized as elongated narrow bands of intense poleward moisture transport and typically associated with extra-tropical cyclones [41, 45, 46]. Previous studies point to a substantial improvement in the representation of AR precipitation in moderately high-resolution models and highlight AR precipitation changes with warming that account for a significant fraction of the total mid-latitude precipitation response, especially over the United States [39, 40, 43, 47–50]. Despite this, initial assessments of moderately high-resolution models for hydrological applications are limited. However, early results show promise in capturing peak annual runoff over the central US when compared to coarser models at or above 100 km grid-spacings, with needs for downscaling and bias correction remaining to accurately assess local scales [51].

Here, we further explore the new opportunities provided from moderately high-resolution to assess changes in river floods and their drivers with warming, distinguishing AR and non-AR precipitation, as well as snow melt, across the continguous United States (CONUS). We utilize the global coupled atmosphere-land model AM4.0/LM4.0 [52, 53] with a resolution of 50 km [40] developed at the Geophysical Fluid Dynamics Laboratory (GFDL), which has shown promising capabilities in capturing mean and extreme precipitation [39, 40, 52]. LM4.0 discharges surface and sub-surface runoff across a grid-scale river network (suppl. Fig. S1) as fluxes of liquid water, ice and

heat to connected grid-cells [54, 55]. This approach benefits from the grid-scale coupling of hydrological processes across river, land and atmospheric domains, allowing for a definitive attribution of various hydrological drivers of high river streamflows indicative of flooding and hence a process-based understanding of their sensitivity to warming.

Our experimental setup (detailed in Sect. 4.1) is designed to isolate the best constrained components of precipitation changes with warming, providing a sound basis for assessing the relation of changes in precipitation and streamflows. First, we isolate the thermodynamic precipitation response to warming, which excludes any changes in atmospheric winds and denotes the most significant and well understood part for how precipitation extremes [10, 56, 57] and AR precipitation [43, 58–60] change with warming. We achieve this by tightly nudging atmospheric winds toward NCEP reanalysis data [61] for both a control and a counter-factual global warming simulation that we run over the historical period of 1951 to 2020. The control simulation (CTRL) follows the CMIP6 HighResMIP protocols [31] and is forced by observed daily sea surface temperatures (SSTs). The counter-factual global warming simulation only differs in SST forcing by a homogeneous increase of SSTs across the global ocean by 2 Kelvin (P2K). Besides isolating the most significant and well constrained parts of the total precipitation response to warming, our nudging approach also minimizes uncertainty arising from natural climate variability as well as dynamically driven model biases (see suppl. Fig. S2), enhancing applicability to hydrological applications. In addition we obtain a day-by-day comparability between the CTRL and P2K simulations as well as with observations (suppl. Fig. S3 and S4), which we exploit in Sect. 2.4.

To elucidate the relationship of precipitation and streamflow changes with warming across CONUS, we first quantify their sensitivities to warming on the mean and in the extremes in Sect. 2.1. We then identify high streamflows and investigate changes in their frequency with warming across CONUS, which we characterize by examining three inter-related conditions for high-flows. Firstly, we attribute high-flows to different upstream water inputs and their changes with warming, distinguishing AR and non-AR precipitation as well as snow-melt in Sect. 2.2. Secondly, we examine changes in water and energy constraints on losses through ET and runoff in Sect. 2.3, highlighting seasonal constraints on the high-flow response. Thirdly, we discuss how these constraints are imprinted on antecedent soil moisture conditions prior to high-flows and to which degree these explain changes in high-flows compared to changes in upstream water inputs in Sect. 2.4. We draw final conclusions in Sect. 3.

2 Results

2.1 Precipitation and streamflow changes with warming

Fig. 1 summarizes the thermodynamically driven changes in precipitation and streamflows across CONUS with warming in our counter-factual warming experiment. The thermodynamic precipitation response manifests as an overall increase across most of CONUS with an average of $3.6\,\%\,\mathrm{K}^{-1}$ (with respect to the global mean warming signal in 2 m temperature), except in the dry southern states Arizona and New Mexico (Fig. 1a). This slightly higher number compared to the typically suggested 2-3 $\%\,\mathrm{K}^{-1}$

[1–4] on the global mean most likely stems from the fact that our warming simulation does not include a CO2 increase, which in itself negatively contributes to the mean response [17, 39, 62].

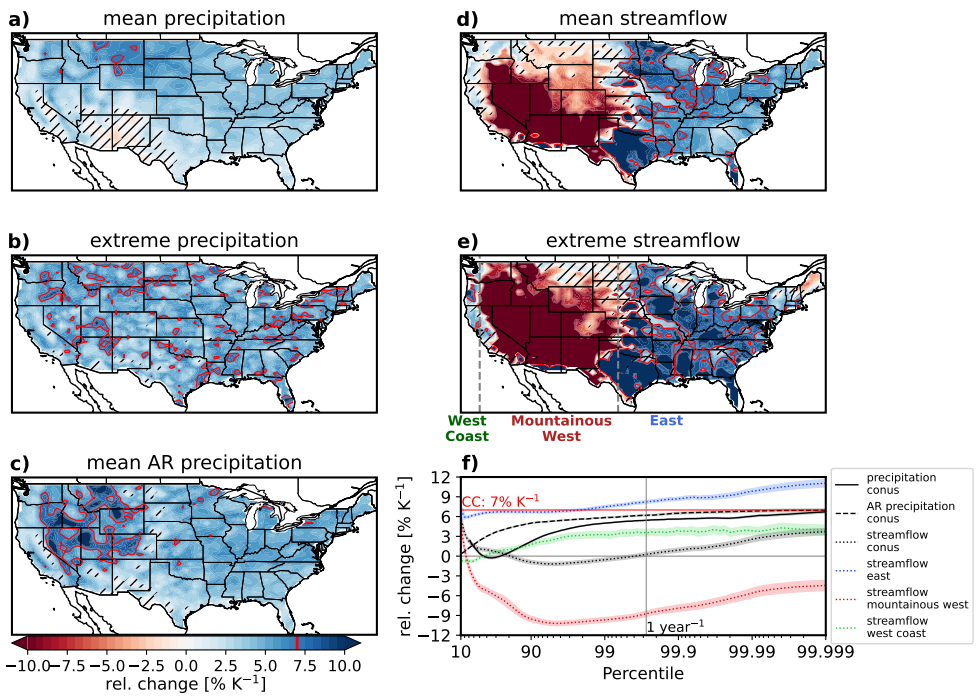


Fig. 1 Changes with warming in (a) mean precipitation, (b) extreme precipitation, (c) mean AR precipitation, (d) mean streamflow and (e) extreme streamflow across CONUS based on counterfactual global warming experiment (see Sect. 4.1). "Extreme" refers the 99.7th percentile of daily values, resembling events with an annual recurrence rate, also indicated by black vertical line in (f). Hatched regions denote insignificant changes of the mean as determined by z-test with critical value $z = 1$. (e) shows relative change with warming in precipitation, AR precipitation and streamflow deduced for each grid-point as function of percentile and then averaged across CONUS (black) and for streamflow also across the west coast (green), the mountainous west (red) and the eastern US (blue) defined by zonal bounds at 120 °W and 100 °W, respectively, indicated by gray dashed lines in (e). Shading denotes standard error across respective region. Red solid line indicates Clausius Clapeyron (CC) scaling of 7 % K^{-1}.

To consider changes in extreme precipitation, we define extreme precipitation as changes in the 99.7th percentile of daily precipitation because it represents an average recurrence rate of once per year, which is commonly used in studies of hydrological extremes [63–66]. Changes in extreme precipitation (Fig. 1b) are positive across CONUS and at 5.4 % K^{-1} generally larger than mean changes, with many local exceedances of the Clausius-Clapeyron (CC) scaling at 7 % K^{-1} [16, 67, 68], highlighting the expected shift towards more intense precipitation [8–15]. Mean AR precipitation changes (Fig. 1c, see Sect. 4.2 on AR detection) fall between mean and

extreme precipitation changes at an average of $4.2\,\%\,\mathrm{K}^{-1}$ but a notably stronger regional pattern with exceedances of CC-scaling across the mountainous west, somewhat resembling the lee-side of the Sierra Nevada, the Cascades and the Rocky Mountains. These results indicate a weakening of the orographic rain shadow with warming, which has previously been predicted from theory [69] and high-resolution regional modeling studies [70–72] and is therefore encouraging to identify in our moderately high-resolution simulations.

The warming response of mean and extreme river streamflows (Fig. 1d+e) strongly differs in its pattern and magnitude from the precipitation response, reflective of the streamflow response being controlled by a multitude of hydrological processes such as antecedent soil conditions and ET [25, 28, 48, 73–77]. Most prominently, mean and extreme streamflows decline over the mountainous western US (regions indicated by gray dashed lines in Fig. 1e and colored text below) in the presence of significant precipitation increases, particularly from ARs. Streamflow declines under warming have previously been noted and linked to the dominance of spring-time snow melt in driving hydrographs [23, 24, 65, 78–80]. Other, more regional studies have identified pronounced increases in evaporative demand [81] and ET [82] across the southwestern US as drivers of drought and dwindling streamflows. Outside the mountainous west streamflows increase with precipitation, however, the increase is significantly stronger over the east than over the west coast (Fig. 1e).

To better conceptualize the identified discrepancies in the relation of the precipitation and streamflow responses to warming, we consider the local surface water balance:

$$P = ET + R + \Delta S \tag{1}$$

At any location, the local input of water through precipitation P is balanced by losses through ET, runoff R and a change in water storage on land ΔS. The local river streamflow is denoted by the streamflow from upstream and the local runoff that in our model is lost inevitably as the river does not feed water back to its surrounding land [53, 55]. Fig. 2a depicts the regionally and annually averaged terms of the surface water balance in the CTRL simulation normalized by the regional mean P. It shows that the partitioning of ET and R across the three regions is vastly different, with R/P denoting only 18 % over the mountainous West, 28 % over the eastern US and 51 % over the west coast. This premise implies that for a given change in the partitioning of ET and R, the relative change in R, and hence streamflows, is most sensitive over the mountainous west and the least sensitive over the west coast.

Fig. 2b shows the absolute change in the partitioning of ET, R and S with respect to P with warming, highlighting the varying responses of each region. We find no noticeable changes over the west coast, in agreement with a scaling of R and streamflows to mostly follow changes in P. Over the mountainous west, we find a substantial increase in ET/P that is balanced by a similar decrease in R/P, explaining the strong relative reduction in streamflows found in Fig. 1d. Over the east, ET/P decreases while R/P increases accordingly, explaining how the diagnosed streamflow increases over the east exceed the increases in P.

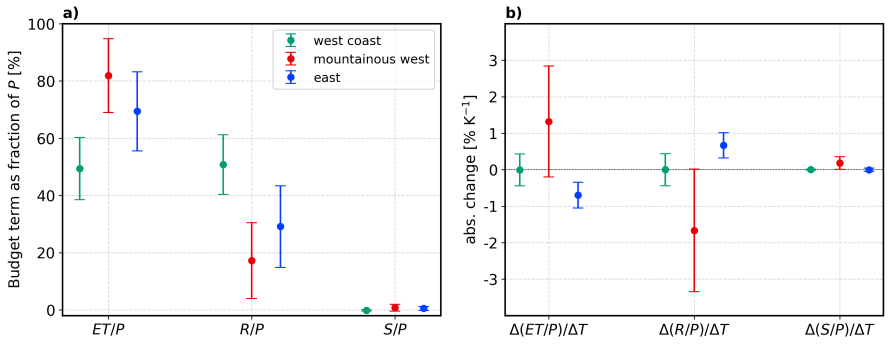


Fig. 2 a) shows regionally averaged terms of the surface water balance (Eq. 1) in the CTRL simulation, normalized by the regional mean precipitation P to make different regions comparable. b) shows the respective change with warming in each of the terms, normalized by the global mean warming response. Note that changes in b) show absolute changes of the budget terms in units of $\%\,\mathrm{K}^{-1}$ due to normalization by P. Errorbars denote spatial standard-deviation within the respective regions.

We summarize the regional discrepancies of extreme precipitation and streamflow changes with warming across sub-regions of CONUS in Fig. 1f by showing mean relative changes in percentiles of the respective quantities (following previous studies [17, 28, 83]). Precipitation changes show an expected increased sensitivity to warming at higher percentiles [4, 10, 17], with AR precipitation being more sensitive than total precipitation [39, 49, 50, 84], approaching CC-scaling for the strongest extremes. Streamflows, however, show a much different behavior in their scaling across percentiles, representative of their loose tie to precipitation. On the one hand, we find an exceedance of precipitation changes by streamflow changes over the eastern US across all percentiles, which exceeds CC-scaling at percentiles > 98. Over the mountainous west, on the other hand, streamflows dwindle across the distribution and even at the highest percentiles where precipitation increases the most. Streamflow changes over the west coast lie in between the other two regions with generally positive changes but at a lower magnitude than CONUS averaged precipitation changes.

2.2 Attribution to upstream precipitation and snow melt

We now further characterize the physical causes for the diagnosed disconnect of precipitation and streamflow changes across CONUS, with particular focus on high-flows. In the following, we identify high-flows as days exceeding the long-term 99.7th percentile of daily streamflow (once-per-year recurrence) based on the CTRL simulation and attribute changes in high-flow frequency with warming to changes in upstream AR precipitation, non-AR precipitation and snow melt across CONUS (see method in Sect. 4.3 and suppl. Fig. S5). We first consider maps of the long-term mean high-flow frequency in Fig. 3 and then point out the regionally varying seasonalities of high-flows and their drivers in Fig. 4.

The first column of Fig. 3 shows the fraction f_{driver} of high-flow events attributed to specific upstream liquid water inputs relative to the total number of attributed high-flow events. The results of the attribution are aggregated over hydrological sub-regions defined through 4-digit hydrological unit codes by the US Geological Survey

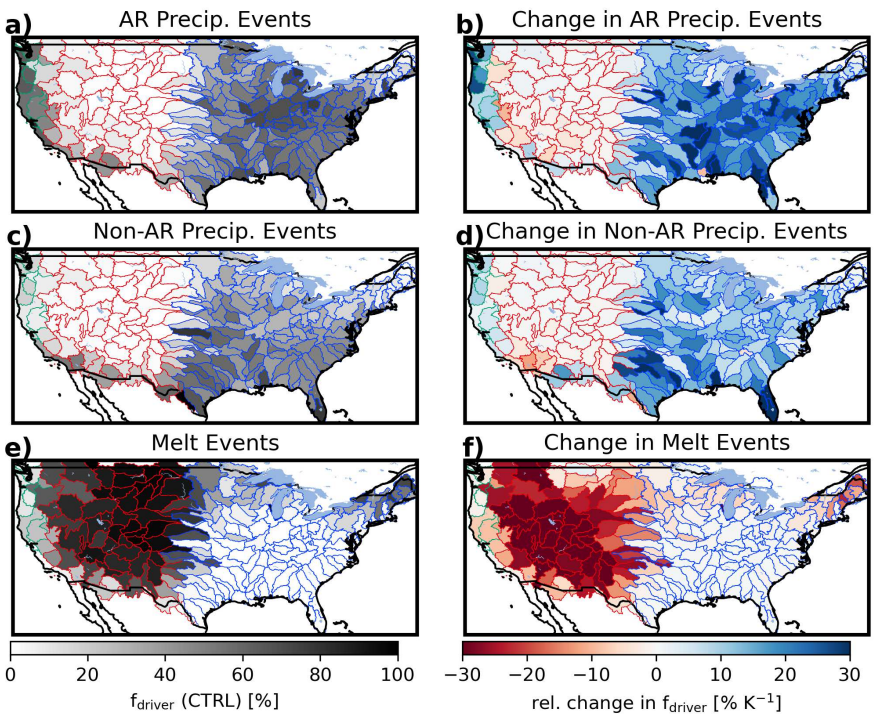


Fig. 3 First column shows fraction f_{driver} of high-flow events attributed to different upstream drivers as relative to total number of attributed high-flows based on CTRL simulation (following attribution method described in Sect. 4.3). Second column shows relative changes in f_{driver} with warming based on P2K-CTRL, normalized by the global mean warming signal. Model results are averaged over HUC4 hydrological sub-regions [85], the outline of which is colored by belonging large-scale region of the west coast (green), the mountainous west (red) and the eastern US (blue)

(USGS)[85]. The separation of hydrological drivers of high streamflows follows a remarkably similar spatial pattern as streamflow changes with warming (Fig. 1d+e), indicative of the hydrological driver being a good predictor of the change in streamflow with warming. We find on the one hand that over both the west coast and eastern US, liquid precipitation is the major driver of high-flows, with AR precipitation exceeding non-AR precipitation in most sub-regions. On the other hand, melt is found as the exclusive driver of high-flows across the mountainous west, also contributing up to 20 % towards high-flow events over some sub-regions of the west coast like the Sacramento river basin and New England in the eastern US.

The second column of Fig. 3 shows the change in the number of high-flow days induced by the respective hydrological drivers with warming in our P2K experiment relative to the CTRL experiment. The pattern of these changes largely resembles the pattern of overall streamflow changes diagnosed in Fig. 1d+e. We find an increasing number of high-flow days across the west coast and the eastern US that we can now attribute to both AR precipitation and to a slightly lower degree non-AR precipitation. Over the mountainous west, we identify a strong reduction in melt induced high-flows

that regionally exceeds -30 % K^{-1}. This reduction in melt-driven high-flows occurs despite strong increases in precipitation over the mountainous west, particularly from ARs (Fig. 1). To start exploring why the reduction in melt driven high-flows over the mountainous west is not buffered by increases in precipitation driven high-flows, while precipitation driven high-flows on the west coast and the eastern US amplify, we now take a seasonal perspective at the changes in high-flows and their drivers. This enables a more process oriented understanding when connecting these results to changes in land-hydrological constraints on ET in the next section.

Fig. 4 shows the regionally and monthly integrated fraction $f^{\text{mon}}_{\text{driver}}$ of high-flows relative to the annual sum of total attributed high-flows for the CTRL simulation (left column) and the P2K − CTRL difference normalized by the global warming signal (right column). The seasonality of total high-flows found in the CTRL simulation (Fig.4a) differs significantly between the three regions. Over the West Coast, high-flows occur most frequently in winter months with a maximum in February. As expected for the west coast [86], the attribution to upstream drivers reveals that the majority of these winter events are driven by ARs with non-AR precipitation playing a secondary role in winter and melt becoming more significant in March. Over the mountainous West, high-flow occurrence peaks in March and is found to be exclusively driven by melt. Over the eastern US, the seasonality is less confined than in the other regions with a broader peak around May. ARs contribute 60 % of high-flows throughout spring while non-AR events become more significant towards summer.

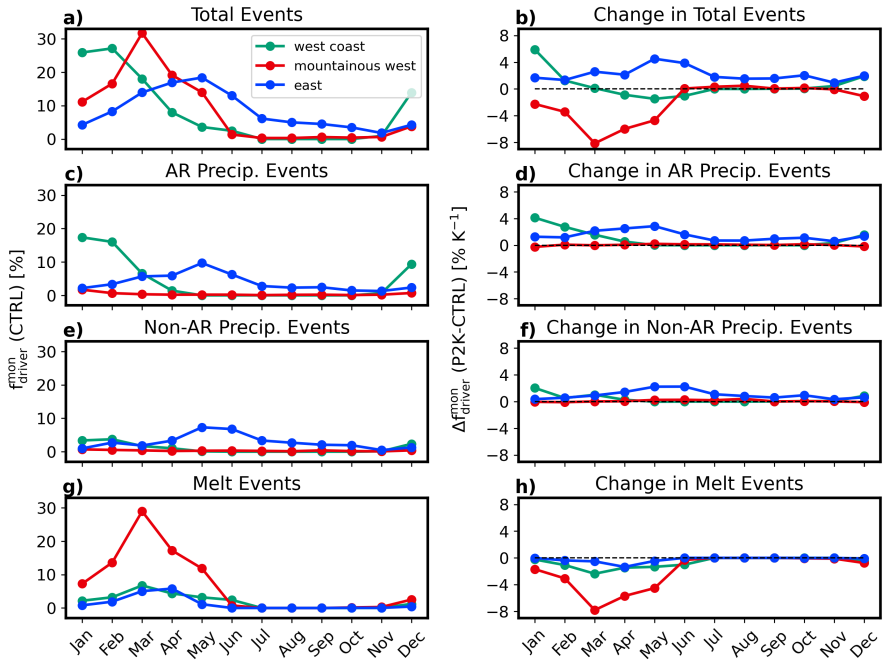


Fig. 4 Regionally and monthly averaged seasonal cycles of high-flow occurrence rates in CTRL simulation (left column) and its change with warming (right column) for total attributed high-flow events (first row) and high-flows driven by AR precipitation (second row), non-AR precipitation (third row) and melt (fourth row).

These regional seasonalities of high-flows change under warming (right column of Fig. 4). Over the west coast, the seasonality becomes more pronounced with more frequent high-flows in winter months and less frequent high-flows in spring driven by more frequent AR-driven high-flows and less frequent melt-driven high-flows. Over the eastern US, high-flow frequency increases throughout the year with a less pronounced maximum in spring, weakening the seasonality of high-flow occurrence with warming. Over the mountainous west, high-flows diminish with warming at a rate that is proportional to the monthly climatological high-flow frequency, also implying a weakened seasonality. It is worth noting that the near-zero change in precipitation-driven high-flows at the annual mean level over the mountainous west (Fig. 3b+d) holds true for the monthly level, i.e. there are no compensating changes in precipitation driven high-flows between different months, despite the previously diagnosed increases in mean and extreme precipitation. This motivates examination of further constraints on high-flows such as changes and the seasonal balance of ET and R that we discuss in the next section.

2.3 Attribution to seasonal constraints on evapotranspiration

We now explore how changes in energy and water constraints on ET with warming help explain changes in the regional variability in changes of the partitioning between

ET and R, as identified in Fig. 2b, and hence the warming response of high-flows. We start by considering annual mean maps of the annual mean dryness index $\mathcal{D}$ and evaporative index $\mathcal{E}$ (as commonly used in Budyko analysis [87, 88]):

$$\mathcal{D} = PET/P \tag{2}$$

$$\mathcal{E} = ET/P \tag{3}$$

where PET refers to potential ET, i.e. the energetic upper bound on ET (see Method Sect. 4.5). An annual mean $\mathcal{D} < 1$ indicates that ET is energy limited while $\mathcal{D} > 1$ indicates that ET is water limited. Fig. 5a shows that annual mean $\mathcal{D}_{CTRL}$ follows a somewhat similar spatial pattern as the streamflow response to warming (Fig. 1d+e) with a strong zonal gradient between energy limited ET in the eastern US and some parts along the west coast and a water limited mountainous west with pronounced aridity in the south-west. This general pattern is in agreement with downscaled reference datasets [89–91].

With an energetic surplus in evaporative potential across the mountainous west, ET is found to increase at a higher rate than over the west coast or eastern US, as implied by a positive change in $\mathcal{E}$ shown in Fig 5b. As previously discussed in Sect. 2.1, the increase in $\mathcal{E}$ across the mountainous west implies a shift of the surface water balance towards overall drier conditions with reduced R. Over the eastern US a slight opposite shift towards enhanced R is found and over the west coast $\mathcal{E}$ changes are only slightly positive. These energetic constraints on annual mean ET align well with the diagnosed annual mean changes in streamflows in Fig. 1.

To more closely examine how the discussed annual mean changes in $\mathcal{D}$ and $\mathcal{E}$ occur in different regions, we now turn to the seasonal perspective and first consider changes in ET and P (Fig. 5c+d). All regions exhibit a pronounced seasonality in P changes with warming, where winter P increases at a higher rate than summer P. This seasonality is particularly pronounced over the mountainous west where mean P increases at around $6\,\%\,\mathrm{K}^{-1}$ in winter and reduces in July and August at around $-1\,\%\,\mathrm{K}^{-1}$. The seasonality in changes of ET (Fig. 5d) is similarly phased as P, however, the relative increase in ET with warming is about double the relative increase in P over the mountainous west and also around one third higher over the west coast in winter while it is slightly weaker over the east.

To consider monthly changes in $\mathcal{D}$ and $\mathcal{E}$, we define them to more appropriately represent the water available for ET on the monthly timescale, which is rather the sum of liquid precipitation P_l and melt M than total precipitation P:

$$\mathcal{D}_m = PET/(P_l + M) \tag{4}$$

$$\mathcal{E}_m = ET/(P_l + M) \tag{5}$$

This definition excludes frozen precipitation that does not melt throughout the month and includes melt that stems from frozen water storage that may have formed through snowfall in months prior.

We find that despite the discussed strong increases of ET in winter, $\mathcal{E}_m$ and $\mathcal{D}_m$ (Fig. 5e+f) reduce in winter months in the eastern US and the mountainous west at up to $-20\,\%\,\mathrm{K}^{-1}$ while increasing in spring. This counter-intuitive result is explained

by seasonal changes to the liquid water supply $P_l + M$, which outweigh the strong changes in ET (see suppl. Fig. S6 and decomposition in suppl. Fig. S8). During winter months, liquid water supply for ET is enhanced with warming as precipitation shifts from frozen to liquid and snow melts throughout the season, shifting the winter-time mountainous west from a water limited ET regime to an energy limited one (triangles in Fig. 5f). During spring, reduced snow-cover reduces melt and hence liquid water supply, increasing $\mathcal{E}_m$ and $\mathcal{D}_m$.

The hydrological regime shift of the winter-time mountainous west towards an energy-limitation of ET occurs despite an enhanced energy supply in winter as shown by the relative change in the net surface energy imbalance F_{net} (Fig. 5g), which we normalize by the latent heat of vaporization $\mathcal{H}_{vap}$ and ET_{CTRL} to obtain comparability to ET changes . The increased F_{net} in winter can largely be attributed to the shortwave component, which is strongly controlled by changes in surface albedo through the loss of reflective snow (suppl. Fig. S6 and S7). This finding is in agreement with previous studies over the western US that argue towards loss of reflective snow energetically fueling ET under warming [82, 92]. Our results highlight how this increased energy-supply for ET is present but dominated by an enhanced water-supply that alters the winter-time mountainous west to an energy-limited ET regime.

Relative changes in winter-time F_{net} in the other regions are weaker than over the mountainous west (Fig. 5g) as the energy balance of the surface is less dominated by snow. In fact, over the eastern US most of the increase in F_{net} is explained through the longwave component, which is mostly driven by the water vapor feedback as cloud changes are small and towards reduced cloud cover in all regions (suppl. Fig. S6+S7). Overall, these less pronounced changes to F_{net} under an already existing energy limitation on ET in the CTRL simulation yield overall weaker responses of ET to warming compared to the mountainous west.

Finally, having discussed the seasonal changes in P and ET with warming across CONUS, we turn to runoff R (Fig. 5h), the direct precursor of streamflows. R changes exhibit a strong seasonality over the mountainous west with increases of around $10\,\%\,\mathrm{K}^{-1}$ in winter and summer and a strong reduction near $20\,\%\,\mathrm{K}^{-1}$ in spring. Considering that in absolute terms most R is produced in spring (suppl. material S7), we find a significant reduction of annual mean R of $-4.1\,\%\,\mathrm{K}^{-1}$. The increase in winter- and summer-time R is nonetheless worth noting given that in both seasons ET is found to increase at a higher rate than P (Fig. 5c+d). In winter months, the increased supply of liquid P and melt explains increases in both R and ET (suppl. Fig. S6). The increase of R in summer despite a reduction in mean P (Fig. 5c) is most likely explained by a shift towards less frequent but more intense P events. Over the west coast, R changes also have a clear seasonal component, albeit at a lower magnitude than over the mountainous west, with increases at up to $5\,\%\,\mathrm{K}^{-1}$ in winter. Over the Eastern US, R increases between 5 to $10\,\%\,\mathrm{K}^{-1}$ throughout the year with a slight variation between a weaker increase in March due to loss of melt and a stronger increase in May due to increased liquid precipitation, particularly from ARs (Fig. 4). The stronger increase in R over the east compared to the west coast can be attributed to the overall stronger increase in P over the east under similar changes in ET, yielding a change in partitioning of P towards increased R/P and reduced ET/P as shown in Fig. 2b.

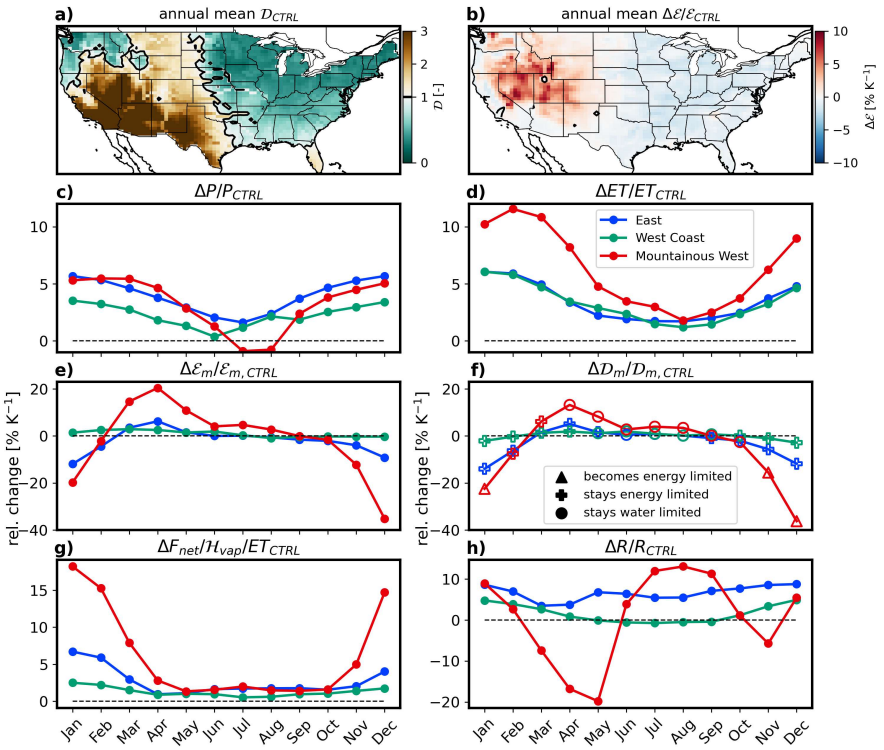


Fig. 5 a) shows annual mean map of $\mathcal{D}$ in CTRL simulation, where PET is derived from Penman-Monteith equation over an open water surface (see method Sect. 4.5). $\mathcal{D}$ <1 indicates energy limitation of ET, and $\mathcal{D}$ >1 indicates water limitation of ET. b) shows annual mean change in $\mathcal{E}$ with warming, indicating whether ET or P is more enhanced with warming. c) to h) show relative changes of mean seasonal cycle c) in P, d) in ET, e) in $\mathcal{E}_m$ (Eq. 5, f) in $\mathcal{D}_m$ (Eq. 4, g) in F_{net}, normalized by specific heat of vaporization $\mathcal{H}_{vap}$ and ET_{CTRL}, h) in R. Relative changes are calculated after spatial averaging.

2.4 Relative importance of changes in antecedent upstream soil moisture and water inputs

With insights gained into the seasonal character of the processes driving changes in P, ET and R across CONUS, we now turn back to changes in high-flows and discuss how these characteristics tie in to changes in antecedent soil moisture, which is often regarded a key predictor for R production [25–28]. Specifically, we examine shifts in antecedent soil saturation $\mathcal{S}_a$ of the top 1 cm of the soil, which describes the degree to which the pores of the soil's top layer are filled with water prior to a precipitation or melt event. The upper-most layer is typically considered for this purpose because it controls production of R at the surface, which during an extreme precipitation or melt event is key for total R production [25]. Our approach is to take advantage of the day-by-day comparability between our CTRL and P2K simulations that is

achieved through tightly nudged atmospheric winds and allows us to separate identified high-flow days into those that occur only in the CTRL simulation, only in the P2K simulation or in both. This way, we can ask across these three categories of events how a change in upstream $\mathcal{S}_a$ conditions may have contributed to a high-flow being only present in either CTRL or P2K, and put this change in relation to changes in the antecedent upstream soil-top water inputs $\mathcal{P}_a$, i.e. the sum of antecedent upstream precipitation and melt (detailed method in Sect. 4.4).

The bottom panels of Fig. 6 depict how many high-flow events, identified on a specific day and location, fall into the different categories of whether it occurred in either only the CTRL or the P2K simulation or in both, showing the total number and its breakdown into the various upstream drivers for each of the CONUS sub-regions. For each of the three categories, the upper panels of Fig. 6 display box-plots for distributions of antecedent upstream conditions ($\mathcal{S}_a$ and $\mathcal{P}_a$) for all high-flow events in the CTRL and P2K simulations. It is evident that the dominant driver of high-flow events and its dependence on the climate state vary strongly across the sub-regions, as would be expected from our previous analysis of Fig. 3. Over the West-Coast, there are few high-flows that only occurred in the CTRL simulation, while most high-flows occur in both CTRL and P2K and are mostly driven by AR precipitation. Those high-flows that only occur in the P2K simulation show slight increases in $\mathcal{P}_a$ and $\mathcal{S}_a$ with warming, both of which act towards enhancing streamflows. As diagnosed in Fig. 4b, the additional high-flows over the west coast in the warmer climate occur mostly in winter during peak AR season, in which enhanced liquid precipitation and earlier snow-melt moistens soils, creating favorable conditions for enhanced runoff.

The strong reduction of high-flows over the mountainous west with warming (Fig. 3) is reflected in the bottom panel of Fig. 6b showing that most high-flows occur only in the CTRL simulation and are induced by melt. Looking at the difference in $\mathcal{S}_a$ and $\mathcal{P}_a$ for these cases between CTRL and P2K, we find that $\mathcal{P}_a$ reduces significantly in the warmer climate while $\mathcal{S}_a$ increases. Hence, the reason many high-flows over the mountainous west in the CTRL simulation do not exist in the P2K simulation is because of the loss of upstream water inputs $\mathcal{P}_a$, in particular snow-melt, which outweighs the increase in increased $\mathcal{S}_a$ that by itself favors high-flows in the P2K simulation. Those high-flows over the mountainous west that are only present in the P2K simulation are samples from a much more even distribution of precipitation and melt induced cases (Fig. 6b, bottom panel), indicating a shift towards a more mixed and less snow-dominated hydrological regime. To a large extent, the newly arising high-flows in the P2K simulation are enabled by significantly enhanced $\mathcal{S}_a$, which on the median increases from 0.2 in CTRL to 0.45 in P2K while the upstream drivers $\mathcal{P}_a$ show a less significant increase. This strong increase in $\mathcal{S}_a$ can be understood as a direct consequence of the discussed reduction in dryness index $\mathcal{D}$ (Fig. 5f) in winter months over the mountainous west with warming.

Over the eastern US, the largest number of high-flows occurs only in the P2K simulation, highlighting the strong sensitivity to warming in this region, which is driven to a similar degree by AR and non-AR precipitation. The high-flows that arise only in the P2K simulation are driven by a shift and a narrowing of the $\mathcal{S}_a$ distribution towards higher $\mathcal{S}_a$ values as well as more extreme $\mathcal{P}_a$, similar to the West Coast but to a more

pronounced degree. The enhanced sensitivity of $\mathcal{S}_a$ over the eastern US compared to the west coast is likely caused by the fact that over the west coast, $\mathcal{S}_a$ is already close to saturation in the CTRL simulation for most high-flows while over the eastern US $\mathcal{S}_a$ increases in winter months as the dryness index $\mathcal{D}_m$ reduces significantly (Fig. 5f).

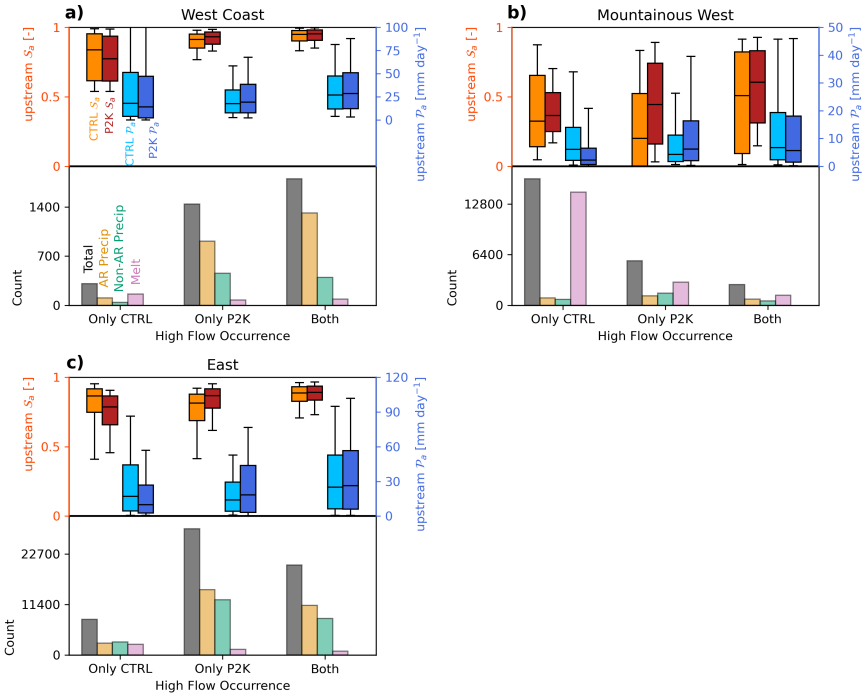


Fig. 6 Bottom panels show regionally integrated (West Coast, Mountainous West, East) distributions of high-flows identified in either CTRL or P2K simulation in categories of whether each high-flow, identified on a specific day and location, only occurred in the CTRL simulation, the P2K simulation or in both. The total number for each category is broken down into the attributed upstream drivers (AR precipitation, non-AR precipitation, melt). Upper panels show box-plots (black line at median, box-bounds at 25th and 75th percentiles, whiskers at 10th and 90th percentiles) of the total distribution (i.e. all upstream drivers) of upstream antecedent soil saturation $\mathcal{S}_a$ (left y-axis) for high-flow events in the CTRL (orange) and the P2K (red) simulations, as well as sum of all upstream drivers $\mathcal{P}_a$ (right y-axis) for high-flow events in the CTRL (light blue) and the P2K (dark blue) simulations in each category.

3 Conclusions

We conducted a counter-factual global warming experiment with the GFDL moderately high-resolution coupled atmosphere-land model AM4.0/LM4.0 to derive physical understanding on the relation of the precipitation and streamflow responses to warming across CONUS, with particular focus on high-flows that are indicative of flooding. By nudging atmospheric winds in both our control and warming simulations, our

approach isolates the thermodynamic component of the total response, focusing attention of this study on the implications of the first order and best constrained part of the total precipitation response on streamflows. We first quantified the precipitation and streamflow responses on the mean and the extremes across CONUS, reconciling their regionally varying relationship through the varying partitioning of ET and R. We then attributed the relation of precipitation and streamflow responses to changes in upstream water inputs, distinguishing AR and non-AR precipitation as well as melt, seasonal energy and water constraints on ET and associated implications for antecedent soil moisture conditions prior to high-flows.

We identify three sub-regions of CONUS that exhibit substantially varying streamflow responses to a comparatively homogeneous precipitation response. Over the West Coast, the streamflow response is positive but falls below precipitation scaling, approaching only up to $4\,\%\,\mathrm{K}^{-1}$ in the extremes. Over the Eastern US, streamflow scales beyond precipitation, approaching $10\,\%\,\mathrm{K}^{-1}$ and over the mountainous western US streamflows dwindle, approaching $-10\,\%\,\mathrm{K}^{-1}$ despite significant increases in annual mean precipitation, particularly from ARs. We associate these regionally varying relationships of the thermodynamic precipitation and streamflow responses to varying hydrological regimes in terms of dominance of snow compared to liquid precipitation as well as energy and water limitations of ET, which are embedded in regionally distinct seasonalities.

The most striking dichotomy between dwindling streamflows across the mountainous west and increasing streamflows elsewhere can be attributed to the dominance of spring-time snow melt in driving the regional hydrological dynamics over the mountainous west. Reduced accumulation of snow throughout winter months diminishes melt in spring, the season of most significant runoff production across the mountainous west. As a consequence of reduced snow-cover in winter, the surface energy balance shifts towards higher PET through enhanced short-wave absorption. At the same time, liquid water supply increases with enhanced winter-time liquid precipitation and melt, yielding an overall moistening of the mountainous west in winter, fueling ET increases at about double the rate of the mean precipitation response and also in winter-time runoff. Through these changes, the winter-time mountainous west shift from a water-limited ET regime to an energy-limited one with warming. We find that the moister soils not only enable enhanced ET, but also create favorable conditions for high-flows during winter at a more even distribution among driving AR precipitation, non-AR precipitation and melt. However, on the annual mean these increases do not balance the significant reduction of melt-driven runoff in spring, resulting in a net annual runoff loss of around $-4.1\,\%\,\mathrm{K}^{-1}$.

While both the eastern US and the west coast exhibit increasing streamflows with warming, the increase is significantly stronger across the East. Over both regions, liquid precipitation is identified as the main driver for high-flows with ARs contributing about two thirds over the west coast and about half over the east while melt plays a secondary role. Our results suggest two major reasons for the difference in the streamflow response between the two regions. Firstly, the partitioning of water losses between ET and R vary significantly between the two regions, with R/P at 51 % over the west-coast and about 28 % over the eastern US. This difference implies a stronger

sensitivity of relative changes in R to changes in the partitioning of ET and P to warming over the east. Secondly, the precipitation increase over the east is simply at a higher magnitude than over the west (Fig. 5c), which in conjunction with almost identical increases in ET must yield a stronger runoff response over the east. This finding is in agreement with previous studies that identify the north-eastern US as the region with the highest precipitation increase over last decades across the US [93–95].

This work highlights the complex system of regionally confined hydrological processes, which result in strongly varying streamflow sensitivities to warming. Changes in upstream water inputs shift the prediction problem of high-flows towards one of precipitation and away from melt, particularly over mountainous regions. ARs are identified as the strongest driver of high-flows across CONUS, not just the west coast, and react sensitively to warming, implying a need for improving predictability of ARs in particular. The presented work isolates the thermodynamic component of the total warming response, which for precipitation extremes is thought to dominate the more uncertain dynamic response, but may not capture significant contributions towards the regional streamflow response. Future research should focus on expanding the framework presented here towards incrementally including the dynamical response, the direct effect of CO2 and its feedback with vegetation, aerosol forcing, as well as changes in SST patterns.

Land surface modelling advances to further reduce approximations of sub-grid heterogeneity and more sophisticated representations of river streamflow dynamics will help reduce uncertainties and more explicitly represent flooding. Another avenue of ongoing development are global storm resolving models (GSRMs) that run at grid-spacings of 5 km and less [96]. While studies of land-atmosphere interactions based on such models are just starting, first results point to significant discrepancies with moderately high-resolution models with regard to the sensitivity of snow-cover to warming in mountainous regions [97]. Further exploring these differences, also in light of the currently simplified assumptions made in the land-schemes of these models, denotes an exciting future perspective.

4 Methods

4.1 Model setup and simulations

We use the coupled land-atmosphere model AM4.0/LM4.0 developed at NOAA's Geophysical Fluid Dynamics Laboratory (GFDL), the main characteristics of which are described in the reference papers [40, 52, 53]. The component models AM4.0 and LM4.0 are extensively used and validated in studying various aspects of the earth system, as they denote integral components of GFDL's modeling suite, namely SPEAR (Seamless System for Prediction and EArth System Research) [98] and CM4 (Climate Model version 4) [99], as well as the physical baseline for more comprehensive representations of dust and chemical interactions within ESM4 (Earth System Model version 4) [100, 101]. A major simplification to those comprehensive modeling systems is that our AM4.0/LM4.0 simulations are forced by observed SSTs and sea ice concentrations, often referred to as AMIP (Atmospheric Model Intercomparison Project) mode

[102], which omits uncertainties revolving around ocean-atmosphere interactions that can result in biases of SST patterns.

We run AM4.0/LM4.0 in a moderately high resolution mode at around 50 km grid-spacing, which on the model's cubic-sphere grid is represented by 192×192 grid-boxes per cube face. This version of the model contributed to the CMIP6 HighResMip experiments [31] and our simulations follow the HighResMip protocol in being forced by daily varying observed SSTs, sea-ice concentrations and radiative gases. One major feature of our simulations is that we nudge atmospheric winds against the 6-hourly NCEP reanalysis [61] to achieve day-by-day comparability to observed weather and between our control and warming simulations, isolating the thermodynamic warming response. We conduct the nudging with a tight nudging timescale of 30 minutes, which assures that there is no significant change in circulation patterns between our control and warming simulations (suppl. Fig. S4). The nudging is applied at a 30 minute time-scale by linearly interpolating the 6-hourly reanalysis data in time to the model timesteps and applying a tendency term to the wind-fields that is proportional to the interpolated NCEP winds and an exponential with an e-folding time of 30 minutes.

Our control (CTRL) and warming (P2K) simulations only differ in forcing by a homogeneous increase of daily SSTs by 2 Kelvin. A realistic future warming pattern can be decomposed into global mean and SST warming patterns. The goal of this study is to focus on the global mean SST warming component, which is robust in both models and observations, although the magnitude of global mean warming in response to a fixed radiative forcing remains uncertain citepsherwood.2020a. Changes in SST warming patterns are challenging to capture in coupled climate models [103, 104], implying uncertainties for precipitation changes with warming patterns [105, 106] that we exclude from the scope of this study.

The land surface model LM4.0 discharges surface and sub-surface runoff across a grid-scale river network as fluxes of liquid water, ice and heat to connected grid-cells following the hydraulic geometry approach [54, 55]. This representation of rivers is idealized by assuming 1-way fluxes with the surrounding land and neglecting effects of inundation. However, for the scope of this study to obtain a regional understanding of mean and high-flow responses to warming, this representation is adequate, given previous evaluation of the model for annual mean runoff [40, 107], runoff ratios [55], and monthly mean peak discharge in the Mississippi [108].

4.2 Atmospheric River Detection

For AR detection, we follow the method of [109], which has previously been applied to AM4.0/LM4.0 simulations, with good agreement to observations [39, 40]. The algorithm is based on 6-hourly mean outputs of zonal and meridional vertically integrated vapor transport (IVT) to compute IVT magnitude at each grid-cell. The climatological seasonal 85th percentile of IVT (considering all 6-hourly timesteps within 5-month intervals centered around respective months) is calculated at each gridcell and used as a threshold to identify possible AR objects, together with a lower absolute limit for IVT of $100\,\mathrm{kg\,m\,s^{-1}}$. Following previous studies [40, 110], we calculate separate IVT thresholds for the CTRL and the P2K simulation to eliminate changes in AR frequency purely due to Clausius-Clapeyron scaling of water vapor content in the atmosphere,

which in itself does not imply enhanced AR activity or impacts. After applying the IVT threshold, geometric conditions are applied to the AR candidate objects, including a minimum AR length > 2000 km, a length-to-width ratio > 2, as well as directional requirements with a minimum poleward component of IVT $> 50\,\mathrm{kg\,m\,s^{-1}}$ and a coherence of IVT direction with more than 50 % of AR-candidate pixels required to have IVT directions within 45° of the mean AR-candidate object direction. The identified AR-objects are stored on 6-hourly timestep. Since for the rest of our analysis we use daily data, we map the 6-hourly AR-masks to daily masks by considering a given day an AR-day if an AR is identified at least once on any of the 6-hourly timesteps.

The resulting climatological contribution of AR precipitation to annual mean and extreme precipitation is found to be very similar between our CTRL simulation and observations across CONUS (suppl. Fig. S10).

4.3 Attribution of high-flows to upstream drivers

We identify daily high-flows from the output of the coupled grid-scale river network that is part of LM4.0 (suppl. Fig. S1). We do so by defining a streamflow threshold based on the long-term 99.7th percentile of daily streamflows at each grid-point in the control simulation, which represents a recurrence interval of once per year. By applying this threshold to both CTRL and P2K simulations, we obtain a database of high-flow days at each location in both simulations. For each of these high-flow days, we conduct an attribution analysis to identify the major upstream source of water that led to the high-flow, distinguishing AR precipitation, non-AR precipitation and snow melt. For a given event, we first identify the upstream area, which for each grid-point is defined by the grid-scale river network. We then calculate the upstream area integral of the potential high-flow drivers so we obtain their upstream time-series. We then conduct a lagged temporal correlation analysis between downstream streamflow at the grid-point where the high-flow occurred and the area-integrated upstream drivers.

To conduct the lagged temporal correlation analysis, we first calculate an event-specific drainage timescale τ_{drain}, which estimates the time it takes for water entering the upstream catchment to drain into the downstream grid-point:

$$\tau_{drain} = \frac{v_{ds}}{\sqrt{A/\pi}} \tag{6}$$

where v_{ds} is the streamflow velocity at the downstream grid-point on the day of the high-flow and A is the upstream area of the catchment. Hence, τ_{drain} represents the time it would take for water in the center of a round catchment with area A to escape the catchment on a straight line at a fixed streamflow velocity v_{ds}. Although this assumption is very crude for estimating the actual drainage time of precipitation entering the catchment, we use it as a starting point for identifying a sufficient correlation of upstream drivers and downstream streamflows.

Knowing τ_{drain} for a given high-flow event, we now iteratively determine the best-correlated upstream driver. We do so by shifting the timeseries of upstream-integrated drivers by $\tau_{shift} \in (0, 1, \ldots, 2 \times \tau_{drain})$ days. For each iteration, we select a temporal window of downstream streamflow and upstream drivers of $\pm\tau_{drain}$ around the day of

high-flow. As a first check of whether a potential upstream driver could have caused the high-flow, we check whether the temporal integral over the selected temporal window of an upstream driver is larger than the temporal integral of streamflow. For example, in the selected window there must have been more precipitation upstream than discharge downstream, if precipitation is to be attributed the main driver of the discharge. We conduct this test for each τ_{shift} and each of the upstream drivers AR-precipitation, non-AR precipitation and melt as well as the sums of AR-precipitation and melt and non-AR precipitation and melt. If for any of these cases, the test is passed, we calculate the temporal correlation coefficient $\rho_{D,S}$ of upstream driver and downstream streamflow in the selected temporal window. If $\rho_{D,S} > 0.8$, we attribute the high-flow event to the particular driver. Note the cases of combined AR- or non-AR precipitation with melt occurred so infrequently in our analysis that we omitted them in our discussions.

A schematic depiction of the attribution method's workflow and some evaluation metrics are provided in suppl. Fig. S5. The method is able to attribute about 35 % of high-flows in both the CTRL and the P2K simulation and works best for grid-points with small upstream basins, which is expected given the idealized assumptions about shape and drainage dynamics of the upstream basin as outlined above through the attribution method.

4.4 Quantifying antecedent soil conditions and upstream drivers

The characterization of antecedent soil saturation is embedded in our attribution method of upstream high-flow drivers (see suppl. Fig. S10). For each high-flow event, we store the timeseries of the area sum of soil moisture at 1 cm depth over the upstream basin, which we call q_s, within the temporal window of $\pm\tau_{drain}$ around the respective high-flow days. Using Eq. 7, we transform q_s into volumetric units, referred to as q_v, which divided by soil porosity φ (Eq. 8) yields soil saturation in 1 cm depth $\mathcal{S}$. Following Eq. 9, we calculate the antecedent upstream soil saturation as the minimum $\mathcal{S}$ within the period leading up to the high-flow event constrained by τ_{drain}.

$$q_v = \frac{q_s}{1000\,\mathrm{kg\,m^{-2}}} \tag{7}$$

$$\mathcal{S} = \frac{q_v}{\varphi} \tag{8}$$

$$\mathcal{S}_a = \min(\mathcal{S}(t)) \quad \text{for } t_{HF} - \tau_{drain} \leq t < t_{HF} \tag{9}$$

To compare $\mathcal{S}_a$ between CTRL and P2K for events that only occur in CTRL and not in P2K or the reverse, we apply our high-flow attribution method based on the CTRL high-flow mask (i.e. identified days and locations of high-flows in CTRL) to the P2K simulation, as well as the P2K high-flow mask to CTRL simulation. This way, we can obtain $\mathcal{S}_a$ for the CTRL and P2K scenario for all events that denote a high-flow only in CTRL, only in P2K or in both.

The sum of upstream drivers $\mathcal{P}_a$, made up of AR precipitation P_{AR}, non-AR precipitation P_{nAR} and melt M, depicted in Fig. 6 is derived analogously to S_a in that we

consider the timeseries of the area-sum of upstream drivers leading up to the high-flow event. However, in this case, we consider the temporal integral of all drivers following Eq. 10.

$$\mathcal{P}_a = \int_{t-\tau_{HF}}^{t_{HF}} (P_{AR} + P_{nAR} + M)\, dt \tag{10}$$

4.5 Calculation of potential evapotranspiration

Potential evapotranspiration (PET) can be considered an energetic upper bound of how much a surface can evaporate given its energy imbalance and in some definitions given specific atmospheric conditions. A wide variety of approaches to calculate PET exist, which are designed for specific vs. more broad applications and that have varying requirements towards the data [111, 112]. Here, we use the widely used Penman-Monteith Equation (Eq. 11) over an open water surface [112] to conduct our analysis of ET changes with warming in Sect. 2.3.

$$\mathrm{PET} = \frac{\Delta}{\Delta+\gamma}\frac{(F_{net}-G)}{L_v} + \frac{\gamma}{\Delta+\gamma}\frac{6.43(1+0.536u)(e_s-e_a)}{L_v} \tag{11}$$

where F_{net} is the radiative surface net energy imbalance, G is the sensible heatflux into the subsurface, both (in units of $\mathrm{MW\,m^{-2}}$); e_a and e_s are the 2 m actual vapor pressure and saturation vapor pressure (kPa); Δ is the derivative of e_s with respect to temperature T ($\mathrm{kPa\,K^{-1}}$); u is the windspeed in 2 m height (m/s); L_v is the latent heat of vaporization ($\mathrm{MJ\,kg^{-1}}$) ; γ is the psychometric constant ($\mathrm{kPa\,K^{-1}}$). These metrics are calculated through the following equations:

$$L_v = 2.501 - 0.002361T \tag{12}$$

$$e_s = 0.6108\exp(17.27T/(T+237.3)) \tag{13}$$

$$\Delta = 4098e_s/(T+237.3)^2 \tag{14}$$

$$\gamma = 0.0016286P/L_v \tag{15}$$

$$u = 0.75\ u_{10\mathrm{m}} \tag{16}$$

where T is 2 m temperature (°C) and P is atmospheric surface pressure (kPa) and $u_{10\mathrm{m}}$ is the windspeed at 10 m height, which is the reference height we obtain as output from the model.

Supplementary information. Supplementary information is available in a separate file.

Acknowledgements. This report was prepared by Marc Prange under awards NA22OAR4050663D and NA23OAR4050431I from the National Oceanic and Atmospheric Administration, U.S. Department of Commerce. The statements, findings, conclusions, and recommendations are those of the author(s) and do not necessarily reflect the views of the National Oceanic and Atmospheric Administration or the U.S. Department of Commerce.

The authors thank Zhihong Tan and Tom Delworth for reading and providing feedback on this manuscript.

References

[1] Allen, M.R., Ingram, W.J.: Constraints on future changes in climate and the hydrologic cycle. Nature **419**(6903), 224–232 (2002) https://doi.org/10.1038/nature01092

[2] Pendergrass, A.G.: The Global-Mean Precipitation Response to CO2-Induced Warming in CMIP6 Models. Geophysical Research Letters **47**(17), 2020–089964 (2020) https://doi.org/10.1029/2020GL089964

[3] Jeevanjee, N., Romps, D.M.: Mean precipitation change from a deepening troposphere. Proceedings of the National Academy of Sciences **115**(45), 11465–11470 (2018) https://doi.org/10.1073/pnas.1720683115

[4] Allan, R.P., Barlow, M., Byrne, M.P., Cherchi, A., Douville, H., Fowler, H.J., Gan, T.Y., Pendergrass, A.G., Rosenfeld, D., Swann, A.L.S., Wilcox, L.J., Zolina, O.: Advances in understanding large-scale responses of the water cycle to climate change. Annals of the New York Academy of Sciences **1472**(1), 49–75 (2020) https://doi.org/10.1111/nyas.14337

[5] Held, I.M., Soden, B.J.: Robust Responses of the Hydrological Cycle to Global Warming. Journal of Climate **19**(21), 5686–5699 (2006) https://doi.org/10.1175/jcli3990.1

[6] Wentz, F.J., Ricciardulli, L., Hilburn, K., Mears, C.: How Much More Rain Will Global Warming Bring? Science **317**(5835), 233–235 (2007) https://doi.org/10.1126/science.1140746

[7] Trenberth, K.E.: Changes in precipitation with climate change. Climate Research **47**(1-2), 123–138 (2011) https://doi.org/10.3354/cr00953

[8] Pall, P., Allen, M.R., Stone, D.A.: Testing the Clausius–Clapeyron constraint on changes in extreme precipitation under CO2 warming. Climate Dynamics **28**(4), 351–363 (2007) https://doi.org/10.1007/s00382-006-0180-2

[9] O'Gorman, P.A., Schneider, T.: The physical basis for increases in precipitation extremes in simulations of 21st-century climate change. Proceedings of the National Academy of Sciences **106**(35), 14773–14777 (2009) https://doi.org/10.

1073/pnas.0907610106

[10] O'Gorman, P.A.: Precipitation Extremes Under Climate Change. Current Climate Change Reports **1**(2), 49–59 (2015) https://doi.org/10.1007/s40641-015-0009-3

[11] Fischer, E.M., Knutti, R.: Observed heavy precipitation increase confirms theory and early models. Nature Climate Change **6**(11), 986–991 (2016) https://doi.org/10.1038/nclimate3110

[12] Papalexiou, S.M., Montanari, A.: Global and Regional Increase of Precipitation Extremes Under Global Warming. Water Resources Research **55**(6), 4901–4914 (2019) https://doi.org/10.1029/2018wr024067

[13] Muller, C., Takayabu, Y.: Response of precipitation extremes to warming: What have we learned from theory and idealized cloud-resolving simulations, and what remains to be learned? Environmental Research Letters **15**(3), 035001 (2020) https://doi.org/10.1088/1748-9326/ab7130

[14] Gimeno, L., Sorí, R., Vázquez, M., Stojanovic, M., Algarra, I., Eiras-Barca, J., Gimeno-Sotelo, L., Nieto, R.: Extreme precipitation events. WIREs Water **9**(6), 1611 (2022) https://doi.org/10.1002/wat2.1611

[15] Bao, J., Stevens, B., Kluft, L., Muller, C.: Intensification of daily tropical precipitation extremes from more organized convection. Science Advances **10**(8), 6801 (2024) https://doi.org/10.1126/sciadv.adj6801

[16] Trenberth, K.E., Dai, A., Rasmussen, R.M., Parsons, D.B.: The Changing Character of Precipitation (2003) https://doi.org/10.1175/BAMS-84-9-1205 . Chap. Bulletin of the American Meteorological Society

[17] Guendelman, I., Merlis, T.M., Cheng, K.-Y., Harris, L.M., Bretherton, C.S., Bolot, M., Zhou, L., Kaltenbaugh, A., Clark, S.K., Fueglistaler, S.: The Precipitation Response to Warming and CO2 Increase: A Comparison of a Global Storm Resolving Model and CMIP6 Models. Geophysical Research Letters **51**(7), 2023–107008 (2024) https://doi.org/10.1029/2023GL107008

[18] Donat, M.G., Delgado-Torres, C., De Luca, P., Mahmood, R., Ortega, P., Doblas-Reyes, F.J.: How Credibly Do CMIP6 Simulations Capture Historical Mean and Extreme Precipitation Changes? Geophysical Research Letters **50**(14), 2022–102466 (2023) https://doi.org/10.1029/2022GL102466

[19] John, A., Douville, H., Ribes, A., Yiou, P.: Quantifying CMIP6 model uncertainties in extreme precipitation projections. Weather and Climate Extremes **36**, 100435 (2022) https://doi.org/10.1016/j.wace.2022.100435

[20] Kim, S., Eghdamirad, S., Sharma, A., Kim, J.H.: Quantification of Uncertainty

in Projections of Extreme Daily Precipitation. Earth and Space Science **7**(8), 2019–001052 (2020) https://doi.org/10.1029/2019EA001052

[21] Tabari, H.: Climate change impact on flood and extreme precipitation increases with water availability. Scientific Reports **10**(1), 13768 (2020) https://doi.org/10.1038/s41598-020-70816-2

[22] Hirabayashi, Y., Mahendran, R., Koirala, S., Konoshima, L., Yamazaki, D., Watanabe, S., Kim, H., Kanae, S.: Global flood risk under climate change. Nature Climate Change **3**(9), 816–821 (2013) https://doi.org/10.1038/nclimate1911

[23] Hamlet, A.F., Lettenmaier, D.P.: Effects of 20th century warming and climate variability on flood risk in the western U.S. Water Resources Research **43**(6) (2007) https://doi.org/10.1029/2006WR005099

[24] Dankers, R., Arnell, N.W., Clark, D.B., Falloon, P.D., Fekete, B.M., Gosling, S.N., Heinke, J., Kim, H., Masaki, Y., Satoh, Y., Stacke, T., Wada, Y., Wisser, D.: First look at changes in flood hazard in the Inter-Sectoral Impact Model Intercomparison Project ensemble. Proceedings of the National Academy of Sciences **111**(9), 3257–3261 (2014) https://doi.org/10.1073/pnas.1302078110

[25] Cao, Q., Mehran, A., Ralph, F.M., Lettenmaier, D.P.: The Role of Hydrological Initial Conditions on Atmospheric River Floods in the Russian River Basin. Journal of Hydrometeorology **20**(8), 1667–1686 (2019) https://doi.org/10.1175/JHM-D-19-0030.1 . Chap. Journal of Hydrometeorology

[26] Cao, Q., Gershunov, A., Shulgina, T., Ralph, F.M., Sun, N., Lettenmaier, D.P.: Floods due to Atmospheric Rivers along the U.S. West Coast: The Role of Antecedent Soil Moisture in a Warming Climate. Journal of Hydrometeorology **21**(8), 1827–1845 (2020) https://doi.org/10.1175/JHM-D-19-0242.1 . Chap. Journal of Hydrometeorology

[27] Ralph, F.M., Waliser, D.E., Dettinger, M.D., Rutz, J.J., Anderson, M.L., Gorodetskaya, I.V., Guan, B., Neff, W.: The Future of Atmospheric River Research and Applications. In: Ralph, F.M., Dettinger, M.D., Rutz, J.J., Waliser, D.E. (eds.) Atmospheric Rivers, pp. 219–247. Springer, Cham (2020). https://doi.org/10.1007/978-3-030-28906-5_8

[28] Sharma, A., Wasko, C., Lettenmaier, D.P.: If Precipitation Extremes Are Increasing, Why Aren't Floods? Water Resources Research **54**(11), 8545–8551 (2018) https://doi.org/10.1029/2018WR023749

[29] Villarini, G., Wasko, C.: Humans, climate and streamflow. Nature Climate Change **11**(9), 725–726 (2021) https://doi.org/10.1038/s41558-021-01137-z

[30] Yu, G., Wright, D.B., Davenport, F.V.: Diverse Physical Processes Drive Upper-Tail Flood Quantiles in the US Mountain West. Geophysical Research Letters **49**(10), 2022–098855 (2022) https://doi.org/10.1029/2022GL098855

[31] Haarsma, R.J., Roberts, M.J., Vidale, P.L., Senior, C.A., Bellucci, A., Bao, Q., Chang, P., Corti, S., Fučkar, N.S., Guemas, V., von Hardenberg, J., Hazeleger, W., Kodama, C., Koenigk, T., Leung, L.R., Lu, J., Luo, J.-J., Mao, J., Mizielinski, M.S., Mizuta, R., Nobre, P., Satoh, M., Scoccimarro, E., Semmler, T., Small, J., von Storch, J.-S.: High Resolution Model Intercomparison Project (HighResMIP v1.0) for CMIP6. Geoscientific Model Development **9**(11), 4185–4208 (2016) https://doi.org/10.5194/gmd-9-4185-2016

[32] Zhang, W., Villarini, G., Scoccimarro, E., Roberts, M., Vidale, P.L., Vanniere, B., Caron, L.-P., Putrasahan, D., Roberts, C., Senan, R., Moine, M.-P.: Tropical cyclone precipitation in the HighResMIP atmosphere-only experiments of the PRIMAVERA Project. Climate Dynamics **57**(1), 253–273 (2021) https://doi.org/10.1007/s00382-021-05707-x

[33] Moreno-Chamarro, E., Caron, L.-P., Ortega, P., Loosveldt Tomas, S., Roberts, M.J.: Can we trust CMIP5/6 future projections of European winter precipitation? Environmental Research Letters **16**(5), 054063 (2021) https://doi.org/10.1088/1748-9326/abf28a

[34] Hariadi, M.H., van der Schrier, G., Steeneveld, G.-J., Sopaheluwakan, A., Tank, A.K., Roberts, M.J., Moine, M.-P., Bellucci, A., Senan, R., Tourigny, E., Putrasahan, D.: Evaluation of onset, cessation and seasonal precipitation of the Southeast Asia rainy season in CMIP5 regional climate models and HighResMIP global climate models. International Journal of Climatology **42**(5), 3007–3024 (2022) https://doi.org/10.1002/joc.7404

[35] Priestley, M.D.K., Catto, J.L.: Improved Representation of Extratropical Cyclone Structure in HighResMIP Models. Geophysical Research Letters **49**(5), 2021–096708 (2022) https://doi.org/10.1029/2021GL096708

[36] Moon, Y., Kim, D., Wing, A.A., Camargo, S.J., Zhao, M., Leung, L.R., Roberts, M.J., Cha, D.-H., Moon, J.: An Evaluation of Tropical Cyclone Rainfall Structures in the HighResMIP Simulations against Satellite Observations (2022) https://doi.org/10.1175/JCLI-D-21-0564.1 . Chap. Journal of Climate

[37] Chen, Q., Ge, F., Jin, Z., Lin, Z.: How well do the CMIP6 HighResMIP models simulate precipitation over the Tibetan Plateau? Atmospheric Research **279**, 106393 (2022) https://doi.org/10.1016/j.atmosres.2022.106393

[38] Liang-Liang, L., Jian, L., Ru-Cong, Y.: Evaluation of CMIP6 HighResMIP models in simulating precipitation over Central Asia. Advances in Climate Change Research **13**(1), 1–13 (2022) https://doi.org/10.1016/j.accre.2021.09.009

[39] Zhao, M.: A Study of AR-, TS-, and MCS-Associated Precipitation and Extreme Precipitation in Present and Warmer Climates. Journal of Climate **35**(2), 479–497 (2022) https://doi.org/10.1175/jcli-d-21-0145.1

[40] Zhao, M.: Simulations of Atmospheric Rivers, Their Variability and Response to GlobalWarming Using GFDL's New High Resolution General Circulation Model. Journal of Climate **33**(23), 1–46 (2020) https://doi.org/10.1175/jcli-d-20-0241.1

[41] Gimeno, L., Nieto, R., Vázquez, M., Lavers, D.: Atmospheric rivers: A mini-review. Frontiers in Earth Science **2** (2014)

[42] McGregor, G.R.: Climate and rivers. River Research and Applications **35**(8), 1119–1140 (2019) https://doi.org/10.1002/rra.3508

[43] Payne, A.E., Demory, M.-E., Leung, L.R., Ramos, A.M., Shields, C.A., Rutz, J.J., Siler, N., Villarini, G., Hall, A., Ralph, F.M.: Responses and impacts of atmospheric rivers to climate change. Nature Reviews Earth & Environment **1**(3), 143–157 (2020) https://doi.org/10.1038/s43017-020-0030-5

[44] Ralph, F.M., Dettinger, M.D.: Storms, floods, and the science of atmospheric rivers. Eos, Transactions American Geophysical Union **92**(32), 265–266 (2011) https://doi.org/10.1029/2011EO320001

[45] Newell, R.E., Newell, N.E., Zhu, Y., Scott, C.: Tropospheric rivers? – A pilot study. Geophysical Research Letters **19**(24), 2401–2404 (1992) https://doi.org/10.1029/92GL02916

[46] Zhang, Z., Ralph, F.M., Zheng, M.: The Relationship Between Extratropical Cyclone Strength and Atmospheric River Intensity and Position. Geophysical Research Letters **46**(3), 1814–1823 (2019) https://doi.org/10.1029/2018GL079071

[47] Chang, P., Zhang, S., Danabasoglu, G., Yeager, S.G., Fu, H., Wang, H., Castruccio, F.S., Chen, Y., Edwards, J., Fu, D., Jia, Y., Laurindo, L.C., Liu, X., Rosenbloom, N., Small, R.J., Xu, G., Zeng, Y., Zhang, Q., Bacmeister, J., Bailey, D.A., Duan, X., DuVivier, A.K., Li, D., Li, Y., Neale, R., Stössel, A., Wang, L., Zhuang, Y., Baker, A., Bates, S., Dennis, J., Diao, X., Gan, B., Gopal, A., Jia, D., Jing, Z., Ma, X., Saravanan, R., Strand, W.G., Tao, J., Yang, H., Wang, X., Wei, Z., Wu, L.: An Unprecedented Set of High-Resolution Earth System Simulations for Understanding Multiscale Interactions in Climate Variability and Change. Journal of Advances in Modeling Earth Systems **12**(12), 2020–002298 (2020) https://doi.org/10.1029/2020MS002298

[48] Liu, X., Chang, P., Fu, D., Saravanan, R., Wang, H., Rosenbloom, N., Zhang, S., Wu, L.: Improved Simulations of Atmospheric River Climatology and Variability in High-Resolution CESM. Journal of Advances in Modeling Earth Systems

14(9), 2022–003081 (2022) https://doi.org/10.1029/2022MS003081

[49] Shields, C.A., Payne, A.E., Shearer, E.J., Wehner, M.F., O'Brien, T.A., Rutz, J.J., Leung, L.R., Ralph, F.M., Marquardt Collow, A.B., Ullrich, P.A., Dong, Q., Gershunov, A., Griffith, H., Guan, B., Lora, J.M., Lu, M., McClenny, E., Nardi, K.M., Pan, M., Qian, Y., Ramos, A.M., Shulgina, T., Viale, M., Sarangi, C., Tomé, R., Zarzycki, C.: Future Atmospheric Rivers and Impacts on Precipitation: Overview of the ARTMIP Tier 2 High-Resolution Global Warming Experiment. Geophysical Research Letters **50**(6), 2022–102091 (2023) https://doi.org/10.1029/2022GL102091

[50] Nellikkattil, A.B., Lee, J.-Y., Guan, B., Timmermann, A., Lee, S.-S., Chu, J.-E., Lemmon, D.: Increased amplitude of atmospheric rivers and associated extreme precipitation in ultra-high-resolution greenhouse warming simulations. Communications Earth & Environment **4**(1), 1–11 (2023) https://doi.org/10.1038/s43247-023-00963-7

[51] Michalek, A.T., Villarini, G., Kim, T., Quintero, F., Krajewski, W.F., Scoccimarro, E.: Evaluation of CMIP6 HighResMIP for Hydrologic Modeling of Annual Maximum Discharge in Iowa. Water Resources Research **59**(8), 2022–034166 (2023) https://doi.org/10.1029/2022WR034166

[52] Zhao, M., Golaz, J.-C., Held, I.M., Guo, H., Balaji, V., Benson, R., Chen, J.-H., Chen, X., Donner, L.J., Dunne, J.P., Dunne, K., Durachta, J., Fan, S.-M., Freidenreich, S.M., Garner, S.T., Ginoux, P., Harris, L.M., Horowitz, L.W., Krasting, J.P., Langenhorst, A.R., Liang, Z., Lin, P., Lin, S.-J., Malyshev, S.L., Mason, E., Milly, P.C.D., Ming, Y., Naik, V., Paulot, F., Paynter, D., Phillipps, P., Radhakrishnan, A., Ramaswamy, V., Robinson, T., Schwarzkopf, D., Seman, C.J., Shevliakova, E., Shen, Z., Shin, H., Silvers, L.G., Wilson, J.R., Winton, M., Wittenberg, A.T., Wyman, B., Xiang, B.: The GFDL Global Atmosphere and Land Model AM4.0/LM4.0: 1. Simulation Characteristics With Prescribed SSTs. Journal of Advances in Modeling Earth Systems **10**(3), 691–734 (2018) https://doi.org/10.1002/2017ms001208

[53] Zhao, M., Golaz, J.-C., Held, I.M., Guo, H., Balaji, V., Benson, R., Chen, J.-H., Chen, X., Donner, L.J., Dunne, J.P., Dunne, K., Durachta, J., Fan, S.-M., Freidenreich, S.M., Garner, S.T., Ginoux, P., Harris, L.M., Horowitz, L.W., Krasting, J.P., Langenhorst, A.R., Liang, Z., Lin, P., Lin, S.-J., Malyshev, S.L., Mason, E., Milly, P.C.D., Ming, Y., Naik, V., Paulot, F., Paynter, D., Phillipps, P., Radhakrishnan, A., Ramaswamy, V., Robinson, T., Schwarzkopf, D., Seman, C.J., Shevliakova, E., Shen, Z., Shin, H., Silvers, L.G., Wilson, J.R., Winton, M., Wittenberg, A.T., Wyman, B., Xiang, B.: The GFDL Global Atmosphere and Land Model AM4.0/LM4.0: 2. Model Description, Sensitivity Studies, and Tuning Strategies. Journal of Advances in Modeling Earth Systems **10**(3), 735–769 (2018) https://doi.org/10.1002/2017MS001209

[54] Leopold, L.B., Jr, T.M.: The hydraulic geometry of stream channels and some physiographic implications. Technical Report 252, U.S. Government Printing Office (1953). https://doi.org/10.3133/pp252

[55] Milly, P.C.D., Malyshev, S.L., Shevliakova, E., Dunne, K.A., Findell, K.L., Gleeson, T., Liang, Z., Phillipps, P., Stouffer, R.J., Swenson, S.: An Enhanced Model of Land Water and Energy for Global Hydrologic and Earth-System Studies. Journal of Hydrometeorology **15**(5), 1739–1761 (2014) https://doi.org/10.1175/jhm-d-13-0162.1

[56] Pfahl, S., O'Gorman, P.A., Fischer, E.M.: Understanding the regional pattern of projected future changes in extreme precipitation. Nature Climate Change **7**(6), 423–427 (2017) https://doi.org/10.1038/nclimate3287

[57] Neelin, J.D., Martinez-Villalobos, C., Stechmann, S.N., Ahmed, F., Chen, G., Norris, J.M., Kuo, Y.-H., Lenderink, G.: Precipitation Extremes and Water Vapor. Current Climate Change Reports **8**(1), 17–33 (2022) https://doi.org/10.1007/s40641-021-00177-z

[58] Gao, Y., Lu, J., Leung, L.R., Yang, Q., Hagos, S., Qian, Y.: Dynamical and thermodynamical modulations on future changes of landfalling atmospheric rivers over western North America. Geophysical Research Letters **42**(17), 7179–7186 (2015) https://doi.org/10.1002/2015GL065435

[59] Mahoney, K., Swales, D., Mueller, M.J., Alexander, M., Hughes, M., Malloy, K.: An Examination of an Inland-Penetrating Atmospheric River Flood Event under Potential Future Thermodynamic Conditions. Journal of Climate **31**(16), 6281–6297 (2018) https://doi.org/10.1175/JCLI-D-18-0118.1 . Chap. Journal of Climate

[60] Zhang, P., Chen, G., Ma, W., Ming, Y., Wu, Z.: Robust Atmospheric River Response to Global Warming in Idealized and Comprehensive Climate Models (2021) https://doi.org/10.1175/JCLI-D-20-1005.1 . Chap. Journal of Climate

[61] Kalnay, E., Kanamitsu, M., Kistler, R., Collins, W., Deaven, D., Gandin, L., Iredell, M., Saha, S., White, G., Woollen, J., Zhu, Y., Chelliah, M., Ebisuzaki, W., Higgins, W., Janowiak, J., Mo, K.C., Ropelewski, C., Wang, J., Leetmaa, A., Reynolds, R., Jenne, R., Joseph, D.: The NCEP/NCAR 40-Year Reanalysis Project (1996). Chap. Bulletin of the American Meteorological Society

[62] Liang, W., Zhao, M., Tan, Z., Knutson, T., Dong, W., Zhang, B.: The Direct Radiative Effect of CO2 Increase on Summer Precipitation in North America. Geophysical Research Letters **51**(14), 2024–109202 (2024) https://doi.org/10.1029/2024GL109202

[63] Berghuijs, W.R., Woods, R.A., Hutton, C.J., Sivapalan, M.: Dominant flood generating mechanisms across the United States. Geophysical Research Letters

43(9), 4382–4390 (2016) https://doi.org/10.1002/2016GL068070

[64] Paltan, H., Waliser, D., Lim, W.H., Guan, B., Yamazaki, D., Pant, R., Dadson, S.: Global Floods and Water Availability Driven by Atmospheric Rivers. Geophysical Research Letters **44**(20), 10387–10395 (2017) https://doi.org/10.1002/2017GL074882

[65] Villarini, G., Zhang, W.: Projected changes in flooding: A continental U.S. perspective. Annals of the New York Academy of Sciences **1472**(1), 95–103 (2020) https://doi.org/10.1111/nyas.14359

[66] Liu, J., Feng, S., Gu, X., Zhang, Y., Beck, H.E., Zhang, J., Yan, S.: Global changes in floods and their drivers. Journal of Hydrology **614**, 128553 (2022) https://doi.org/10.1016/j.jhydrol.2022.128553

[67] Lenderink, G., Barbero, R., Loriaux, J.M., Fowler, H.J.: Super-Clausius–Clapeyron Scaling of Extreme Hourly Convective Precipitation and Its Relation to Large-Scale Atmospheric Conditions (2017) https://doi.org/10.1175/JCLI-D-16-0808.1 . Chap. Journal of Climate

[68] Martinkova, M., Kysely, J.: Overview of Observed Clausius-Clapeyron Scaling of Extreme Precipitation in Midlatitudes. Atmosphere **11**(8), 786 (2020) https://doi.org/10.3390/atmos11080786

[69] Siler, N., Roe, G.: How will orographic precipitation respond to surface warming? An idealized thermodynamic perspective. Geophysical Research Letters **41**(7), 2606–2613 (2014) https://doi.org/10.1002/2013GL059095

[70] Siler, N., Durran, D.: What Causes Weak Orographic Rain Shadows? Insights from Case Studies in the Cascades and Idealized Simulations. Journal of the Atmospheric Sciences **73**(10), 4077–4099 (2016) https://doi.org/10.1175/JAS-D-15-0371.1 . Chap. Journal of the Atmospheric Sciences

[71] Koszuta, M., Siler, N., Leung, L.R., Wettstein, J.J.: Weakened Orographic Influence on Cool-Season Precipitation in Simulations of Future Warming Over the Western US. Geophysical Research Letters **51**(2), 2023–107298 (2024) https://doi.org/10.1029/2023GL107298

[72] Hughes, M., Swales, D., Scott, J.D., Alexander, M., Mahoney, K., McCrary, R.R., Cifelli, R., Bukovsky, M.: Changes in extreme integrated water vapor transport on the U.S. west coast in NA-CORDEX, and relationship to mountain and inland precipitation. Climate Dynamics **59**(3), 973–995 (2022) https://doi.org/10.1007/s00382-022-06168-6

[73] Ivancic, T.J., Shaw, S.B.: Examining why trends in very heavy precipitation should not be mistaken for trends in very high river discharge. Climatic Change **133**(4), 681–693 (2015) https://doi.org/10.1007/s10584-015-1476-1

[74] Musselman, K.N., Lehner, F., Ikeda, K., Clark, M.P., Prein, A.F., Liu, C., Barlage, M., Rasmussen, R.: Projected increases and shifts in rain-on-snow flood risk over western North America. Nature Climate Change **8**(9), 808–812 (2018) https://doi.org/10.1038/s41558-018-0236-4

[75] Berghuijs, W.R., Harrigan, S., Molnar, P., Slater, L.J., Kirchner, J.W.: The Relative Importance of Different Flood-Generating Mechanisms Across Europe. Water Resources Research **55**(6), 4582–4593 (2019) https://doi.org/10.1029/2019WR024841

[76] Albano, C.M., Dettinger, M.D., Harpold, A.A.: Patterns and Drivers of Atmospheric River Precipitation and Hydrologic Impacts across the Western United States. Journal of Hydrometeorology **21**(1), 143–159 (2020) https://doi.org/10.1175/JHM-D-19-0119.1 . Chap. Journal of Hydrometeorology

[77] Welty, J., Zeng, X.: Characteristics and Causes of Extreme Snowmelt over the Conterminous United States (2021) https://doi.org/10.1175/BAMS-D-20-0182.1 . Chap. Bulletin of the American Meteorological Society

[78] Hirabayashi, Y., Kanae, S., Emori, S., Oki, T., Kimoto, M.: Global projections of changing risks of floods and droughts in a changing climate. Hydrological Sciences Journal **53**(4), 754–772 (2008) https://doi.org/10.1623/hysj.53.4.754

[79] Do, H.X., Mei, Y., Gronewold, A.D.: To What Extent Are Changes in Flood Magnitude Related to Changes in Precipitation Extremes? Geophysical Research Letters **47**(18), 2020–088684 (2020) https://doi.org/10.1029/2020GL088684

[80] Zhang, S., Zhou, L., Zhang, L., Yang, Y., Wei, Z., Zhou, S., Yang, D., Yang, X., Wu, X., Zhang, Y., Li, X., Dai, Y.: Reconciling disagreement on global river flood changes in a warming climate. Nature Climate Change **12**(12), 1160–1167 (2022) https://doi.org/10.1038/s41558-022-01539-7

[81] McEvoy, D.J., Pierce, D.W., Kalansky, J.F., Cayan, D.R., Abatzoglou, J.T.: Projected Changes in Reference Evapotranspiration in California and Nevada: Implications for Drought and Wildland Fire Danger. Earth's Future **8**(11), 2020–001736 (2020) https://doi.org/10.1029/2020EF001736

[82] Milly, P.C.D., Dunne, K.A.: Colorado River flow dwindles as warming-driven loss of reflective snow energizes evaporation. Science **367**(6483), 1252–1255 (2020) https://doi.org/10.1126/science.aay9187

[83] Wasko, C., Sharma, A.: Global assessment of flood and storm extremes with increased temperatures. Scientific Reports **7**(1), 7945 (2017) https://doi.org/10.1038/s41598-017-08481-1

[84] Wang, S., Ma, X., Zhou, S., Wu, L., Wang, H., Tang, Z., Xu, G., Jing, Z., Chen,

Z., Gan, B.: Extreme atmospheric rivers in a warming climate. Nature Communications **14**(1), 3219 (2023) https://doi.org/10.1038/s41467-023-38980-x

[85] Jones, K.A., Niknami, L.S., Buto, S.G., Decker, D.: Federal Standards and Procedures for the National Watershed Boundary Dataset (WBD): Chapter 3 of Section A, Federal Standards, Book 11, Collection And Delineation of Spatial Data. Techniques and Methods. US Geological Survey, ??? (2022)

[86] Ralph, F.M., Coleman, T., Neiman, P.J., Zamora, R.J., Dettinger, M.D.: Observed Impacts of Duration and Seasonality of Atmospheric-River Landfalls on Soil Moisture and Runoff in Coastal Northern California. Journal of Hydrometeorology **14**(2), 443–459 (2013) https://doi.org/10.1175/JHM-D-12-076.1 . Chap. Journal of Hydrometeorology

[87] Budyko, M.I., Miller, D.H.: Climate and life (1974)

[88] Trancoso, R., Larsen, J.R., McAlpine, C., McVicar, T.R., Phinn, S.: Linking the Budyko framework and the Dunne diagram. Journal of Hydrology **535**, 581–597 (2016) https://doi.org/10.1016/j.jhydrol.2016.02.017

[89] Heidari, H., Arabi, M., Warziniack, T., Kao, S.-C.: Assessing Shifts in Regional Hydroclimatic Conditions of U.S. River Basins in Response to Climate Change over the 21st Century. Earth's Future **8**(10), 2020–001657 (2020) https://doi.org/10.1029/2020EF001657

[90] Young, A.M., Friedl, M.A., Novick, K., Scott, R.L., Moon, M., Frolking, S., Li, X., Carrillo, C.M., Richardson, A.D.: Disentangling the Relative Drivers of Seasonal Evapotranspiration Across a Continental-Scale Aridity Gradient. Journal of Geophysical Research: Biogeosciences **127**(8), 2022–006916 (2022) https://doi.org/10.1029/2022JG006916

[91] Zomer, R.J., Xu, J., Trabucco, A.: Version 3 of the Global Aridity Index and Potential Evapotranspiration Database. Scientific Data **9**(1), 409 (2022) https://doi.org/10.1038/s41597-022-01493-1

[92] Ban, Z., Xin, C., Fang, Y., Ma, X., Li, D., Lettenmaier, D.P.: Snowmelt-Radiation Feedback Impact on Western U.S. Streamflow. Geophysical Research Letters **50**(23), 2023–105118 (2023) https://doi.org/10.1029/2023GL105118

[93] Kunkel, K.E., Karl, T.R., Brooks, H., Kossin, J., Lawrimore, J.H., Arndt, D., Bosart, L., Changnon, D., Cutter, S.L., Doesken, N., Emanuel, K., Groisman, P.Y., Katz, R.W., Knutson, T., O'Brien, J., Paciorek, C.J., Peterson, T.C., Redmond, K., Robinson, D., Trapp, J., Vose, R., Weaver, S., Wehner, M., Wolter, K., Wuebbles, D.: Monitoring and Understanding Trends in Extreme Storms: State of Knowledge. Bulletin of the American Meteorological Society **94**(4), 499–514 (2013) https://doi.org/10.1175/bams-d-11-00262.1

[94] Easterling, D.R., Arnold, J.R., Knutson, T., Kunkel, K.E., LeGrande, A.N., Leung, L.R., Vose, R.S., Waliser, D.E., Wehner, M.F.: Ch. 7: Precipitation Change in the United States. Climate Science Special Report: Fourth National Climate Assessment, Volume I. Technical report, U.S. Global Change Research Program (2017). https://doi.org/10.7930/J0H993CC

[95] Jong, B.-T., Delworth, T.L., Cooke, W.F., Tseng, K.-C., Murakami, H.: Increases in extreme precipitation over the Northeast United States using high-resolution climate model simulations. npj Climate and Atmospheric Science **6**(1), 18 (2023) https://doi.org/10.1038/s41612-023-00347-w

[96] Stevens, B., Satoh, M., Auger, L., Biercamp, J., Bretherton, C.S., Chen, X., Düben, P., Judt, F., Khairoutdinov, M., Klocke, D., Kodama, C., Kornblueh, L., Lin, S.-J., Neumann, P., Putman, W.M., Röber, N., Shibuya, R., Vanniere, B., Vidale, P.L., Wedi, N., Zhou, L.: DYAMOND: The DYnamics of the Atmospheric general circulation Modeled On Non-hydrostatic Domains. Progress in Earth and Planetary Science **6**(1), 61 (2019) https://doi.org/10.1186/s40645-019-0304-z

[97] Hsieh, T.-L., Harris, L., Cheng, K.-Y., Kaltenbaugh, A., Zhou, L., Jia, L., Zhao, M.: Western United States wintertime precipitation response to warming: An assessment in a global storm-resolving model. Climate Dynamics **63**(3), 165 (2025) https://doi.org/10.1007/s00382-025-07651-6

[98] Delworth, T.L., Cooke, W.F., Adcroft, A., Bushuk, M., Chen, J.-H., Dunne, K.A., Ginoux, P., Gudgel, R., Hallberg, R.W., Harris, L., Harrison, M.J., Johnson, N., Kapnick, S.B., Lin, S.-J., Lu, F., Malyshev, S., Milly, P.C., Murakami, H., Naik, V., Pascale, S., Paynter, D., Rosati, A., Schwarzkopf, M.d., Shevliakova, E., Underwood, S., Wittenberg, A.T., Xiang, B., Yang, X., Zeng, F., Zhang, H., Zhang, L., Zhao, M.: SPEAR: The Next Generation GFDL Modeling System for Seasonal to Multidecadal Prediction and Projection. Journal of Advances in Modeling Earth Systems **12**(3), 2019–001895 (2020) https://doi.org/10.1029/2019MS001895

[99] Held, I.M., Guo, H., Adcroft, A., Dunne, J.P., Horowitz, L.W., Krasting, J., Shevliakova, E., Winton, M., Zhao, M., Bushuk, M., Wittenberg, A.T., Wyman, B., Xiang, B., Zhang, R., Anderson, W., Balaji, V., Donner, L., Dunne, K., Durachta, J., Gauthier, P.P.G., Ginoux, P., Golaz, J.-C., Griffies, S.M., Hallberg, R., Harris, L., Harrison, M., Hurlin, W., John, J., Lin, P., Lin, S.-J., Malyshev, S., Menzel, R., Milly, P.C.D., Ming, Y., Naik, V., Paynter, D., Paulot, F., Ramaswamy, V., Reichl, B., Robinson, T., Rosati, A., Seman, C., Silvers, L.G., Underwood, S., Zadeh, N.: Structure and Performance of GFDL's CM4.0 Climate Model. Journal of Advances in Modeling Earth Systems **11**(11), 3691–3727 (2019) https://doi.org/10.1029/2019MS001829

[100] Dunne, J.P., Horowitz, L.W., Adcroft, A.J., Ginoux, P., Held, I.M., John, J.G., Krasting, J.P., Malyshev, S., Naik, V., Paulot, F., Shevliakova, E., Stock, C.A.,

Zadeh, N., Balaji, V., Blanton, C., Dunne, K.A., Dupuis, C., Durachta, J., Dussin, R., Gauthier, P.P.G., Griffies, S.M., Guo, H., Hallberg, R.W., Harrison, M., He, J., Hurlin, W., McHugh, C., Menzel, R., Milly, P.C.D., Nikonov, S., Paynter, D.J., Ploshay, J., Radhakrishnan, A., Rand, K., Reichl, B.G., Robinson, T., Schwarzkopf, D.M., Sentman, L.T., Underwood, S., Vahlenkamp, H., Winton, M., Wittenberg, A.T., Wyman, B., Zeng, Y., Zhao, M.: The GFDL Earth System Model Version 4.1 (GFDL-ESM 4.1): Overall Coupled Model Description and Simulation Characteristics. Journal of Advances in Modeling Earth Systems **12**(11), 2019–002015 (2020) https://doi.org/10.1029/2019MS002015

[101] Horowitz, L.W., Naik, V., Paulot, F., Ginoux, P.A., Dunne, J.P., Mao, J., Schnell, J., Chen, X., He, J., John, J.G., Lin, M., Lin, P., Malyshev, S., Paynter, D., Shevliakova, E., Zhao, M.: The GFDL Global Atmospheric Chemistry-Climate Model AM4.1: Model Description and Simulation Characteristics. Journal of Advances in Modeling Earth Systems **12**(10), 2019–002032 (2020) https://doi.org/10.1029/2019MS002032

[102] Gates, W.L.: AN AMS CONTINUING SERIES: GLOBAL CHANGE–AMIP: The Atmospheric Model Intercomparison Project (1992). Chap. Bulletin of the American Meteorological Society

[103] Seager, R., Henderson, N., Cane, M.: Persistent Discrepancies between Observed and Modeled Trends in the Tropical Pacific Ocean (2022) https://doi.org/10.1175/JCLI-D-21-0648.1 . Chap. Journal of Climate

[104] Kang, S.M., Shin, Y., Kim, H., Xie, S.-P., Hu, S.: Disentangling the mechanisms of equatorial Pacific climate change. Science Advances **9**(19), 5059 (2023) https://doi.org/10.1126/sciadv.adf5059

[105] Zhang, S., Stier, P., Dagan, G., Zhou, C., Wang, M.: Sea surface warming patterns drive hydrological sensitivity uncertainties. Nature Climate Change **13**(6), 545–553 (2023) https://doi.org/10.1038/s41558-023-01678-5

[106] Zhao, M., Knutson, T.: Crucial role of sea surface temperature warming patterns in near-term high-impact weather and climate projection. npj Climate and Atmospheric Science **7**(1), 1–13 (2024) https://doi.org/10.1038/s41612-024-00681-7

[107] Lee, M., Malyshev, S., Shevliakova, E., Milly, P.C.D., Jaffé, P.R.: Capturing interactions between nitrogen and hydrological cycles under historical climate and land use: Susquehanna watershed analysis with the GFDL land model LM3-TAN. Biogeosciences **11**(20), 5809–5826 (2014) https://doi.org/10.5194/bg-11-5809-2014

[108] Wiel, K., Kapnick, S.B., Vecchi, G.A., Smith, J.A., Milly, P.C.D., Jia, L.: 100-Year Lower Mississippi Floods in a Global Climate Model: Characteristics and Future Changes. Journal of Hydrometeorology **19**(10), 1547–1563 (2018) https:

//doi.org/10.1175/JHM-D-18-0018.1 . Chap. Journal of Hydrometeorology

[109] Guan, B., Waliser, D.E.: Detection of atmospheric rivers: Evaluation and application of an algorithm for global studies. Journal of Geophysical Research: Atmospheres **120**(24), 12514–12535 (2015) https://doi.org/10.1002/2015JD024257

[110] Shields, C.A., Kiehl, J.T.: Atmospheric river landfall-latitude changes in future climate simulations. Geophysical Research Letters **43**(16), 8775–8782 (2016) https://doi.org/10.1002/2016GL070470

[111] Milly, P.C.D., Dunne, K.A.: Potential evapotranspiration and continental drying. Nature Climate Change **6**(10), 946–949 (2016) https://doi.org/10.1038/nclimate3046

[112] Milly, P.c.d., Dunne, K.A.: A Hydrologic Drying Bias in Water-Resource Impact Analyses of Anthropogenic Climate Change. JAWRA Journal of the American Water Resources Association **53**(4), 822–838 (2017) https://doi.org/10.1111/1752-1688.12538

Supplementary Files

This is a list of supplementary files associated with this preprint. Click to download.

- npjpapersupplmprangesub.pdf